ARTICLE

Location Effect in a Photocatalytic Hybrid System of Metal-Organic Framework Interfaced with Semiconductor Nanoparticles

Qi-chao Shang[a,b], Xin-zuo Fang[a,c], Hai-long Jiang[a,c], Qun Zhang[a,b*]

a. Hefei National Laboratory for Physical Sciences at the Microscale, School of Chemistry and Materials Science, University of Science and Technology of China, Hefei 230026, China
b. Department of Chemical Physics, Synergetic Innovation Center of Quantum Information & Quantum Physics, University of Science and Technology of China, Hefei 230026, China
c. Department of Chemistry, CAS Key Laboratory of Soft Matter Chemistry, Collaborative Innovation Center of Suzhou Nano Science and Technology, University of Science and Technology of China, Hefei 230026, China

(Dated: Received on March 20, 2018; Accepted on April 9, 2018)

We report an ultrafast spectroscopy investigation that addresses the subtle location effect in a prototypical semiconductor-MOF hybrid system with TiO_2 nanoparticles being incorporated inside or supported onto $Cu_3(BTC)_2$, denoted as TiO_2@$Cu_3(BTC)_2$ and TiO_2/$Cu_3(BTC)_2$, respectively. By tracking in real time the interface electron dynamics in the hybrid system, we find that the interface states formed between TiO_2 and $Cu_3(BTC)_2$ can act as an effective relay for electron transfer, whose efficiency rests on the relative location of the two components. It is such a subtle location effect that brings on difference in photocatalytic CO_2 reduction using the two semiconductor-MOF hybrids. The mechanistic understanding of the involved interface electron-transfer behavior and effect opens a helpful perspective for rational design of MOF-based hybrid systems for photoelectrochemical applications.

Key words: Metal-organic framework, Photocatalysis, Ultrafast spectroscopy, Transient absorption

I. INTRODUCTION

Metal-organic frameworks (MOFs), a class of porous coordination polymers formed by metal ions and organic ligands, have shown great promise in photoelectrochemical applications due to their unique properties such as high specific surface areas, outstanding porosity, and structural diversity [1−3]. MOF-based heterogeneous composites, in which metal or semiconductor nanoparticles (NPs) are interfaced with a MOF material, have been exploited to optimize the desired performance in photocatalysis [4−10]. Recently, in a prototypical metal-MOF hybrid system, *i.e.*, platinum (Pt) NPs interfaced with UiO-66-NH_2, we revealed that the Pt location (*i.e.*, either incorporated inside or supported onto the MOF) can significantly influence the photocatalytic efficiency for hydrogen production [6]. In this case the MOF functions as an electron donor while the Pt NPs serve as a co-catalyst, facilitating electron transfer and promoting charge separation therein. During the carrier-transfer process within heterostructures, MOFs could act as either electron donors [4−6] or electron acceptors [7−10]. Notably, it would be more beneficial when the MOF behaves as an electron acceptor in the hybrid system given that the MOF offers extensive active sites for photocatalysis [11]. Recent efforts have been made to develop semiconductor-MOF hybrid systems, in which the MOF receives electrons donated by the interfaced semiconductor component [7−10].

It is interesting to see if the location effect observed in metal-MOF system also manifests in semiconductor-MOF system. A useful way to examine this is to track in real time the interface electron dynamics in the system by ultrafast optical spectroscopy [12−16]. To this end, we have performed a set of femtosecond (fs) time-resolved transient absorption (TA) measurements on a typical semiconductor-MOF system with TiO_2 NPs being incorporated inside or supported onto $Cu_3(BTC)_2$ (BTC=benzene-1,3,5-tricarboxylate), forming the two composites denoted TiO_2@$Cu_3(BTC)_2$ and TiO_2/$Cu_3(BTC)_2$, respectively. Analysis of our fs-TA results revealed that the interface states formed between TiO_2 and $Cu_3(BTC)_2$ can serve as an effective relay for electron transfer, whose efficiency is highly dependent on the relative location of the two components. It is such a subtle location effect that leads to their different photocatalytic performances in CO_2 reduction.

*Author to whom correspondence should be addressed.
E-mail: qunzh@ustc.edu.cn

 ©2018 Chinese Physical Society

II. EXPERIMENTS

A. Materials

Polyvinylpyrrolidone (PVP, M_W=29000) and 1,3,5-benzenetricarboxylic acid (H_3BTC) were purchased from Sigma-Aldrich. Cuprous oxide (Cu_2O) was purchased from Alfa Aesar. Tetrabutyl titanate, *N*, *N*-dimethylformamide (DMF), and ethanol were purchased from Sinopharm Chemical Reagent Co., Ltd. All of the chemicals were used as received without further purification.

B. Synthesis of the samples

1. Synthesis of TiO_2

1 mL tetrabutyl titanate was added into a Pyrex vial. The vial was then placed into an oven and kept at 85 °C. The precursor, tetrabutyl titanate, was hydrolyzed smoothly and the resulting white powders were dehydrated to yield the amorphous sample of TiO_2 NPs.

2. Synthesis of $Cu_3(BTC)_2$

1.48 g PVP was dissolved in 10 mL pure water and heated at 70 °C under magnetic stirring. 8 mL of DMF containing 21 mg H_3BTC was added into the PVP solution, which was heated for 10 min. Then, 2 mL of DMF containing 5.6 mg Cu_2O was added and further heated at 70 °C for 30 min. The product was washed with ethanol three times to remove PVP. The resulting product was dispersed in ethanol again. After 2 h the supernatant was taken out and centrifuged to obtain the $Cu_3(BTC)_2$ microcrystals.

3. Synthesis of TiO_2@$Cu_3(BTC)_2$

5 mg $Cu_3(BTC)_2$ was activated by evacuation at 130 °C for 1 day in a Pyrex reaction tube. After being cooled to room temperature, $Cu_3(BTC)_2$ was immersed with 1 mL tetrabutyl titanate under evacuation for another day. Subsequently, the sample was removed from the Schlenk flask and washed with ethanol to remove tetrabutyl titanate on the surface. Finally, the sample was dried to yield the TiO_2@$Cu_3(BTC)_2$ composites.

4. Synthesis of TiO_2/$Cu_3(BTC)_2$

5 mg $Cu_3(BTC)_2$ was dispersed in 1 mL ethanol, and then 50 L tetrabutyl titanate was added into ethanol under stirring. The mixture was dehydrated quickly to yield the TiO_2/$Cu_3(BTC)_2$ composites.

C. Characterization

1. Routine characterizations

The concentrations of Ti and Cu were measured with a Thermo Scientific Plasma Quad III inductively coupled plasma mass spectrometry (ICP-MS) with the samples being dissolved in HCl/HNO_3 (3:1, *V*:*V*). The sample morphology of TiO_2, $Cu_3(BTC)_2$, TiO_2@$Cu_3(BTC)_2$, and TiO_2/$Cu_3(BTC)_2$ was examined by transmission electron microscopy (TEM, JEOL-2010). Prior to electron microscopy characterizations, a drop of the aqueous suspension of particles was placed onto a piece of carbon-coated copper grid or silicon wafer and dried under ambient conditions. Powder X-ray diffraction (XRD) was carried out on a Japan Rigaku Smart Lab rotation anode X-ray diffractometer equipped with graphite monochromatized Cu Kα radiation (λ=1.54 Å). The X-ray photoelectron spectroscopy (XPS) characterization was performed on a Thermo Scientific ESCALAB 250 X-ray photoelectron spectrometer, using nonmonochromatized Al Kα X-ray as the excitation source. The expected charging of samples was corrected by setting the C 1s binding energy of the adventitious carbon to 284.5 eV. The steady-state UV-Vis diffuse reflectance spectra (270−510 nm) were recorded on a Shimadzu Solid Spec-3700 spectrophotometer (reference: $BaSO_4$).

2. Ultrafast spectroscopy

The fs-TA measurements were performed under ambient conditions in an integrated Helios spectrometer (Ultrafast Systems LLC) with pump and probe beams derived from an amplified femtosecond laser system (Coherent). The 320-nm pump pulses (∼50 nJ/pulse at the sample cell) were delivered by a travelling-wave optical parametric amplifier system (TOPAS-800-fs), which was excited by a Ti:sapphire regenerative amplifier (Legend Elite-1K-HE; 800 nm, 35 fs, 3 mJ/pulse, and 1 kHz repetition rate) seeded with a mode-locked Ti:sapphire laser system (Micra 5) and then pumped with an Nd:YLF laser (Evolution 30). The pump power was adjusted through a series of neutral-density filter wheels. The stable white-light continuum (WLC) probe pulses (450−650 nm) were generated by attenuating and focusing the 800-nm beam (split from the regenerative amplifier, ∼400 nJ/pulse) onto a sapphire crystal plate. To correct the pulse-to-pulse fluctuation of the WLC, the WLC was split into a probe beam and a reference beam. The time delays between the pump and probe pulses were controlled by a motorized optical delay line. The instrument response function (IRF) was determined to be ∼100 fs by measuring solvent responses under the same experimental conditions (with the exception of a higher excitation power). A mechanical synchronized chopper operating at 500 Hz was used to modulate the pump pulses such that the fs-

DOI:10.1063/1674-0068/31/cjcp1803044 ©2018 Chinese Physical Society

TA spectra with and without the pump pulses can be recorded alternately. The temporal and spectral profiles (chirp corrected) of the pump-induced differential transmission of the WLC probe light (*i.e.*, absorbance change) were visualized by an optical fiber-coupled multichannel spectrometer (with a complementary metal-oxide-semiconductor sensor) and further processed by the Surface Xplorer software equipped with the Helios system. The samples were well dispersed in a mixture of spectrum-pure acetonitrile (CH_3CN) and ethylene glycol. The solution was contained in a 0.7-mL sealed quartz cuvette under a continuous magnetic stirring condition, ensuring that the photoexcited volume of the sample was kept fresh during the fs-TA measurements.

3. Photocatalytic tests

The photocatalytic CO_2 reduction tests were carried out in a 100-mL optical reaction vessel under stirring at ambient temperature using a 300-W Xe lamp as the light source. In addition, a 400-nm short-wave-pass cut-off filter was used. The catalyst (10 mg) was dispersed in CH_3CN (19 mL) with 1 mL triethanolamine (TEOA) being added as a sacrificial reagent. The mixture was bubbled with CO_2 under stirring for 40 min. The product was measured by a gas chromatograph (Shimadzu GC-2014, nitrogen as carrier gas), during which 200 μL of the product was injected and quantified by a calibration plot against the internal CO standard.

III. RESULTS AND DISCUSSION

The two composites with an identical mass ratio of TiO_2 over $Cu_3(BTC)_2$ (*i.e.*, ∼0.2) were prepared based on the pre-synthesized $Cu_3(BTC)_2$ product. TEM images (FIG. 1) revealed that the MOF morphology (*i.e.*, octahedron-shaped $Cu_3(BTC)_2$ microcrystal with a lateral size of ∼800 nm) was well maintained upon being integrated with TiO_2 NPs. As for TiO_2@$Cu_3(BTC)_2$, one can see that the surfaces of $Cu_3(BTC)_2$ were very smooth (FIG. 1(a)) and TiO_2 NPs were well confined within the $Cu_3(BTC)_2$ (FIG. 1(b), which is an enlarged view of the selected region in FIG. 1(a)). In contrast, as for $TiO_2/Cu_3(BTC)_2$, the surfaces of $Cu_3(BTC)_2$ were rough and covered with TiO_2 NPs (FIG. 1 (c) and (d)). The excellent encapsulation of TiO_2 NPs inside MOF for TiO_2@$Cu_3(BTC)_2$ and nearly uniform coverage of TiO_2 with MOF for $TiO_2/Cu_3(BTC)_2$ clearly indicated the different locations of TiO_2 NPs for the two composites. FIG. 2 shows the comparison of the size distribution of TiO_2 NPs in TiO_2@$Cu_3(BTC)_2$ and $TiO_2/Cu_3(BTC)_2$, which shows no significant difference, precluding the possible impact of size distribution of TiO_2 NPs on the interface electron dynamics in the hybrid systems. Moreover, the observation of nearly

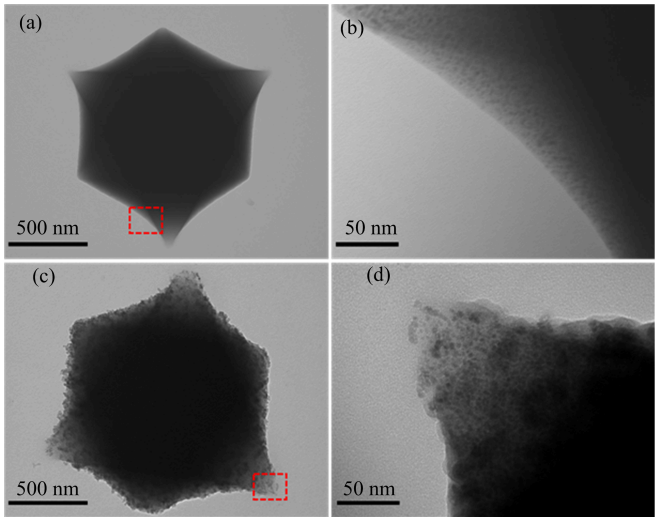

FIG. 1 Typical TEM images for the two hybrid systems under investigation: (a, b) TiO_2@$Cu_3(BTC)_2$ and (c, d) $TiO_2/Cu_3(BTC)_2$. Panels (b) and (d) are the enlarged views of the selected regions (red rectangles) in panels (a) and (c), respectively.

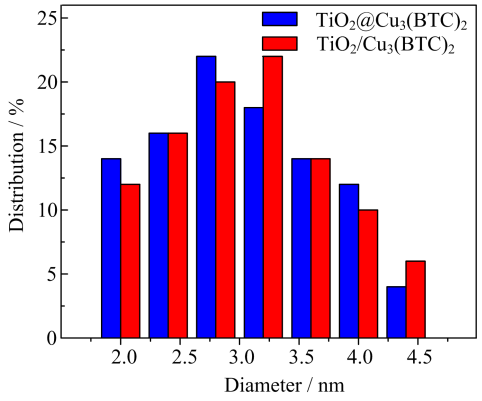

FIG. 2 Comparison of the size distribution of TiO_2 NPs in TiO_2@$Cu_3(BTC)_2$ and $TiO_2/Cu_3(BTC)_2$.

identical powder XRD patterns (FIG. 3) suggested that the crystalline structure of $Cu_3(BTC)_2$ was well maintained for the two composites.

FIG. 4 exhibits the valence-band (VB) XPS spectra recorded on the two composites and the two bare samples of TiO_2 and $Cu_3(BTC)_2$. The VB edges for TiO_2 and $Cu_3(BTC)_2$ were determined to be at 2.74 and 2.25 eV, respectively, below the Fermi level. Notably, both composites turned out to hold an identical VB edge at 1.92 eV below the Fermi level, suggesting that the different loading locations of TiO_2 NPs in the composites would not bring on significant modification for the electronic structures and properties of $Cu_3(BTC)_2$. The survey and high resolution XPS spectra recorded on the two composites can be found in FIG. S1 in the supplementary materials.

To track the real-time photoexcited electron dynam-

DOI:10.1063/1674-0068/31/cjcp1803044 ©2018 Chinese Physical Society

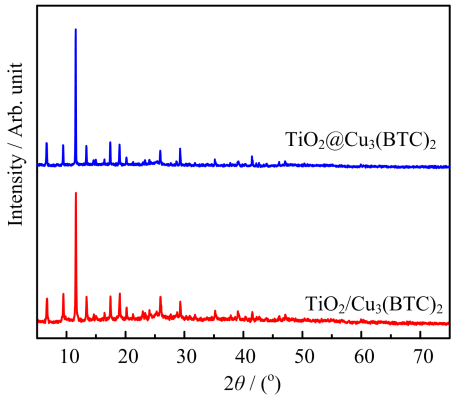

FIG. 3 Powder XRD patterns recorded on TiO_2@$Cu_3(BTC)_2$ and TiO_2/$Cu_3(BTC)_2$, showing no obvious difference.

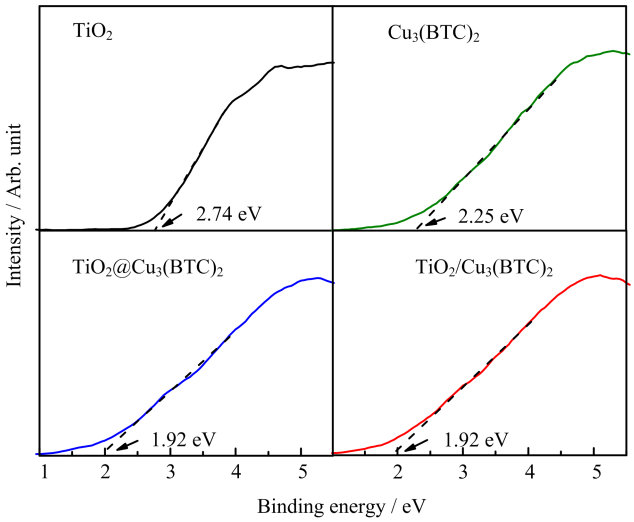

FIG. 4 Valence-band XPS spectra recorded on the two composite samples of TiO_2@$Cu_3(BTC)_2$ and TiO_2/$Cu_3(BTC)_2$ as well as the two bare samples of TiO_2 and $Cu_3(BTC)_2$.

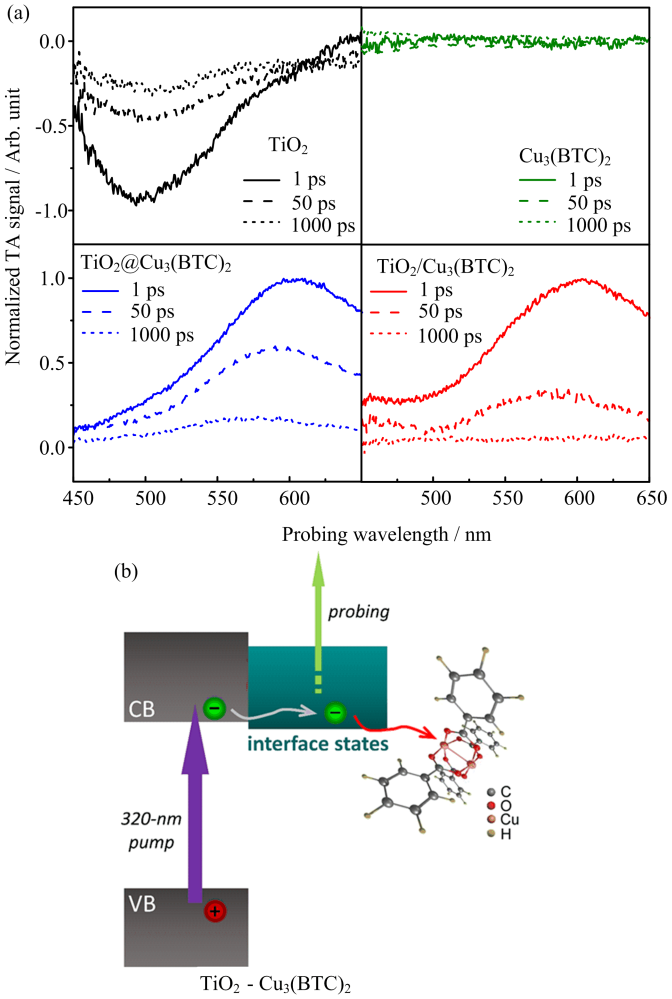

FIG. 5 (a) Representative fs-TA spectra (pump at 320 nm) for the two hybrid systems (lower panels) and for the two reference systems (upper panels). (b) Schematic illustration of the interface electro-transfer processes in the semiconductor-MOF hybrid system.

ics in the two hybrid systems, we performed fs-TA spectroscopy characterization. A routine pump-probe configuration with an ultraviolet (UV) pump (320 nm) and a white-light continuum probe (450−650 nm) was adopted. The 320-nm photoexcitation (∼3.88 eV) is suited to induce interband transition in TiO_2 (bandgap ∼3.2 eV). FIG. 5(a) displays the fs-TA spectra taken at several representative probe delays for the two composite samples (lower panels) and two reference samples (upper panels). Bare $Cu_3(BTC)_2$ exhibits nearly indiscernible fs-TA signal as compared to bare TiO_2, echoing to their steady-state UV-Vis absorption spectra (see FIG. S2 in the supplementary materials). Markedly, the negative probe bleach (PB) signal of bare TiO_2 is completely reversed to the positive photoinduced absorption (PA) signal upon being interfaced with $Cu_3(BTC)_2$. As for bare TiO_2, the PB evolution probed in 450−650 nm, a red-shifted region relative to the 320-nm pump, tracks via stimulated emission the population of photoexcited electrons in its conduction band (CB) [13, 15]. As for the two hybrid systems, however, the PA evolution observed in the same region should not correspond to the excited-state absorption (*i.e.*, upward probing) from the CB electrons on the TiO_2 side, but rather reflects that of the electrons transferred rapidly from the CB of TiO_2 to the interface states formed between TiO_2 and $Cu_3(BTC)_2$. There should occur a sort of efficient TiO_2-to-$Cu_3(BTC)_2$ interface electron-transfer process, given that the photoexcited component is dominantly TiO_2 instead of $Cu_3(BTC)_2$. The mechanistic picture is illustrated in FIG. 5(b).

To gain more insights into the interface electron transfer and the subsequent relaxation processes in the hybrid systems, we turn our attention to the involved PA kinetics. FIG. 6 exhibits a set of representative fs-TA kinetics data taken at 560 nm. As for bare TiO_2,

DOI:10.1063/1674-0068/31/cjcp1803044 ©2018 Chinese Physical Society

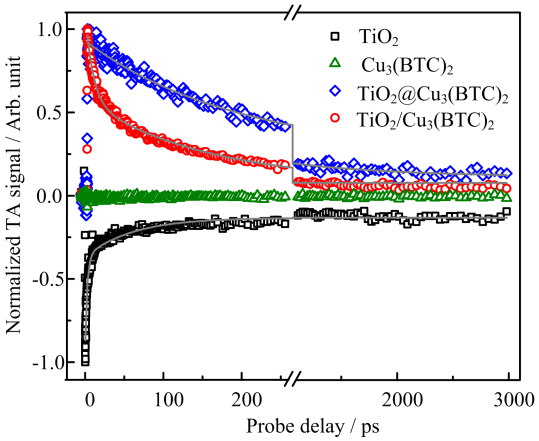

FIG. 6 Representative fs-TA kinetics (pump at 320 nm, probe at 560 nm) for the two hybrid systems as well as for the two reference systems.

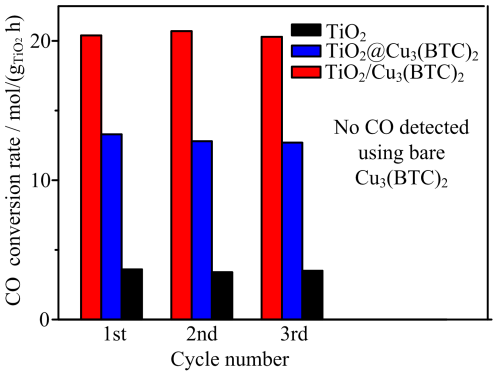

FIG. 7 CO conversion rates for TiO_2, TiO_2@$Cu_3(BTC)_2$, and $TiO_2/Cu_3(BTC)_2$ in the recycling tests of photocatalytic CO_2 reduction. The product mole yields were calibrated against the 15-mg photoactive TiO_2. Signals for by-products were indiscernible.

the negative PB signal builds up within the instrument response function (IRF) of ∼100 fs and then recovers with an average lifetime of ∼110 ps. The fast build-up (<100 fs) reflects the initial generation and cooling of hot excitons, while the following recovery (∼110 ps) accounts for the subsequent exciton trapping and recombination [12, 17]. Also, the early-time build-up for the two hybrid systems occurs within the IRF, suggesting that the interface electron-transfer process therein is extremely fast (indicated by a grey, wiggly arrow in FIG. 5(b)). Strikingly, the subsequent relaxation, which should be linked to the event that the promptly accumulated interface-state electrons are redistributed into the electron acceptor states of $Cu_3(BTC)_2$ (indicated by a red, wiggly arrow in FIG. 5(b)), exhibits a pronounced difference: τ_1=(182±16) ps (69.1%) and τ_2=(1006±323) ps (30.9%) (or (769±292) ps on average) for TiO_2@$Cu_3(BTC)_2$, while τ_1=10.1±1.1 ps (51.2%) and τ_2=(157±7) ps (48.8%) (or (148±6) ps on average) for $TiO_2/Cu_3(BTC)_2$. A roughly 5-fold acceleration (in terms of average lifetime) was detected for $TiO_2/Cu_3(BTC)_2$ relative to TiO_2@$Cu_3(BTC)_2$. This evidences that the interface states formed between semiconductor and MOF can act as an effective relay for semiconductor-to-MOF electron transfer, whose efficiency is highly dependent on the relative location of the two components. In the current case, such a relay effect in the system with TiO_2 NPs being supported onto $Cu_3(BTC)_2$ (*i.e.*, $TiO_2/Cu_3(BTC)_2$) was proven more efficient than in the system with TiO_2 NPs being incorporated inside $Cu_3(BTC)_2$ (*i.e.*, TiO_2@$Cu_3(BTC)_2$), suggesting that the coupling between the interface states and the electron acceptor states of MOF is stronger in $TiO_2/Cu_3(BTC)_2$ than in TiO_2@$Cu_3(BTC)_2$.

Considering that the higher efficiency in interface states-mediated electron transfer would promote electron-hole separation (on the photoexcited semiconductor side) and electron redistribution (on the electron-accepting MOF side), we anticipated that $TiO_2/Cu_3(BTC)_2$ could achieve a better photocatalytic performance than TiO_2@$Cu_3(BTC)_2$. This expectation was verified by a set of photocatalytic CO_2 reduction tests, in which $TiO_2/Cu_3(BTC)_2$ was found to stand out among others (FIG. 7). Notably, the two composites were found to possess an identical mass ratio of TiO_2 NPs over $Cu_3(BTC)_2$ (*i.e.*, ∼0.2) and a similar size distribution of TiO_2 NPs (FIG. 2), as discussed above. On the basis of these observations, it is safe to conclude that the difference in photocatalytic performance for the two composite samples should not simply be due to the slight differences in the loading distribution and density of TiO_2 NPs, but rather related to the different interface electron-transfer efficiencies for the two samples.

IV. CONCLUSION

We have presented an ultrafast spectroscopy investigation addressing the subtle location effect in a prototypical semiconductor-MOF hybrid system with TiO_2 nanoparticles being incorporated inside or supported onto $Cu_3(BTC)_2$, denoted TiO_2@$Cu_3(BTC)_2$ and $TiO_2/Cu_3(BTC)_2$, respectively. By tracking in real time the interface electron dynamics in the hybrid system, we find that the interface states formed between TiO_2 and $Cu_3(BTC)_2$ can act as an effective relay for electron transfer, whose efficiency rests on the relative location of the two components. Such a subtle location effect is responsible for the performance difference in photocatalytic CO_2 reduction using the two hybrid systems. The mechanistic insights into the involved interface electron-transfer effect provide a helpful perspective for rational design of MOF-based hybrid systems for photoelectrochemical applications.

DOI:10.1063/1674-0068/31/cjcp1803044 ©2018 Chinese Physical Society

Supplementary materials: XPS spectra and steady-state UV-Vis absorption spectra of the samples are available in the supplementary materials.

V. ACKNOWLEDGMENTS

This work was supported by the Ministry of Science and Technology of China (No.2016YFA0200602), the National Natural Science Foundation of China (No.21573211 and No.21633007), and the Fundamental Research Funds for the Central Universities of China (No.WK2340000063).

[1] H. C. Zhou, J. R. Long, and O. M. Yaghi, Chem. Rev. **112**, 673 (2012).
[2] P. Falcaro, R. Ricco, A. Yazdi, I. Imaz, S. Furukawa, D. Maspoch, R. Ameloot, J. D. Evans, and C. Doonan, Coord. Chem. Rev. **307**, 237 (2016).
[3] Q. H. Yang, Q. Xu, and H. L. Jiang, Chem. Soc. Rev. **46**, 4774 (2017).
[4] C. Wang, K. E. deKrafft, and W. B. Lin, J. Am. Chem. Soc. **134**, 7211 (2012).
[5] L. Y. Chen, Y. Peng, H. Wang, Z. Z. Gu, and C. Y. Duan, Chem. Commun. **50**, 8651 (2014).
[6] J. D. Xiao, Q. C. Shang, Y. J. Xiong, Q. Zhang, Y. Luo, S. H. Yu, and H. L. Jiang, Angew. Chem. Int. Ed. **55**, 9389 (2016).
[7] R. Li, J. H. Hu, M. S. Deng, H. L. Wang, X. J. Wang, Y. L. Hu, H. L. Jiang, J. Jiang, Q. Zhang, Y. Xie, and Y. J. Xiong, Adv. Mater. **26**, 4783 (2014).
[8] S. B. Wang and X. C. Wang, Appl. Catal. B **162**, 494 (2015).
[9] L. Shi, T. Wang, H. B. Zhang, K. Chang, and J. H. Ye, Adv. Funct. Mater. **25**, 5360 (2015).
[10] D. A. Giannakoudakis, N. A. Travlou, J. Secor, and T. J. Bandosz, Small **13**, 1601758 (2017).
[11] J. Y. Lee, O. K. Farha, J. Roberts, K. A. Scheidt, S. B. T. Nguyen, and J. T. Hupp, Chem. Soc. Rev. **38**, 1450 (2009).
[12] D. A. Wheeler and J. Z. Zhang, Adv. Mater. **25**, 2878 (2013).
[13] S. Bai, J. Jiang, Q. Zhang, and Y. J. Xiong, Chem. Soc. Rev. **44**, 2893 (2015).
[14] B. Pattengale, S. Z. Yang, J. Ludwig, Z. Q. Huang, X. Y. Zhang, and J. E. Huang, J. Am. Chem. Soc. **138**, 8072 (2016).
[15] Q. Zhang and Y. Luo, High Power Laser Sci. Eng. **4**, e22 (2016).
[16] Q. Y. Li and T. Q. Lian, Nano Lett. **17**, 3152 (2017).
[17] W. A. Tisdale, K. J. Williams, B. A. Timp, D. J. Norris, E. S. Aydil, and X. Y. Zhu, Science **328**, 1543 (2010).

DOI:10.1063/1674-0068/31/cjcp1803044 ©2018 Chinese Physical Society